scientific reports

OPEN

Antimonate sequestration from aqueous solution using zirconium, iron and zirconium-iron modified biochars

Md. Aminur Rahman[1,3], Mohammad Mahmudur Rahman[1], Md. Mezbaul Bahar[1], Peter Sanderson[1] & Dane Lamb[2✉]

Antimony (Sb) is increasingly being recognized as an important contaminant due to its various industrial applications and mining operations. Environmental remediation approaches for Sb are still lacking, as is the understanding of Sb environmental chemistry. In this study, biosolid biochar (BSBC) was produced and utilized to remove antimonate (Sb(V)) from aqueous solution. Zirconium (Zr), Zirconium-iron (Zr–Fe) and Fe–O coated BSBC were synthesized for enhancing Sb(V) sorption capacities of BSBC. The combined results of specific surface area, FTIR, SEM–EDS, TEM–EDS, and XPS confirmed that Zr and/or Zr–Fe were successfully coated onto BSBC. The effects of reaction time, pH, initial Sb(V) concentration, adsorbate doses, ionic strength, temperature, and the influence of major competitive co-existing anions and cations on the adsorption of Sb(V) were investigated. The maximum sorption capacity of Zr–O, Zr–Fe, Zr–FeCl$_3$, Fe–O, and FeCl$_3$ coated BSBC were 66.67, 98.04, 85.47, 39.68, and 31.54 mg/g respectively under acidic conditions. The XPS results revealed redox transformation of Sb(V) species to Sb(III) occurred under oxic conditions, demonstrating the biochar's ability to behave as an electron shuttle during sorption. The sorption study suggests that Zr–O and Zr–O–Fe coated BSBC could perform as favourable adsorbents for mitigating Sb(V) contaminated waters.

Anthropogenic activities such as mining, smelting and metallurgy, combustion of fossil fuels, production of flame-retardants, catalysis of plastic production, semiconductors, amongst others, are increasingly important sources of antimony (Sb) in the environment[1,2]. Antimony contamination has received growing attention primarily due to its increasing industrial applications and the relatively limited knowledge on environmental toxicity, transformations and fate in the environment[3,4]. In natural waters, Sb exists in both trivalent (Sb(III)) and pentavalent (Sb(V)) oxidation states. Trivalent Sb mainly exists as $Sb(OH)_3^0$ and $SbO(OH)^0$ at pH 2–10, in the form of SbO^+ and $Sb(OH)_2^+$ at pH < 2, but can also can be present as SbO_2^- and $Sb(OH)_4^+$ at pH > 10.4. Pentavalent Sb exists mainly as $Sb(OH)_6^-$ at pH > 2.7[5,6]. The toxicity and mobility depends on the Sb oxidation state, with Sb(III) exhibiting tenfold greater toxicity than Sb(V)[7–9]. In addition, antimony trioxide (Sb_2O_3) has been identified as a carcinogenic to humans (Group 2B) by IARC[10].

Considering the increasing threat posed by Sb in the environment, several technologies have been trialled to remove excess Sb from natural waters. Remediation technologies to date rely on (ad)sorption, coagulation, electrocoagulation, co-precipitation, electrodeposition and membrane techniques[11]. Due to the expensive operational and maintenance costs involved in such processes, most of these techniques have limitations in removing Sb. The adsorption process has emerged as a promising and viable approach due to its economical nature, high efficiency, simplicity, technical flexibility, and social acceptability[12,13].

Several adsorbents have been investigated for Sb removal from natural and industrial waters, including multiwalled carbon nanotubes[14], hydrated ferric oxide supported by calcite sand[15], graphene[16], Fe-modified aerobic granules[17], and Fe–Mn binary oxide[18]. The adsorption capacity of these materials tends to be poor. Only a few sorbents such as metal-loaded Zr(IV), Fe(III) saponified orange waste[19], zero-valent iron nanoparticles coatings on aluminum and silicon minerals[20,21], iron oxyhydroxides, zirconium oxide (Zr–O)-carbon nanofibers[13],

[1]Global Centre for Environmental Remediation (GCER), The University of Newcastle, Callaghan, Australia. [2]Global Innovation Centre for Advanced Nanomaterials, The University of Newcastle, Advanced Technology Centre - Room 181, University Drive, Callaghan, NSW 2308, Australia. [3]Department of Public Health Engineering (DPHE), Zonal Laboratory, Khulna 9100, Bangladesh. ✉email: dane.lamb@newcastle.edu.au

reduced graphene oxide/Mn_3O_4[22], MnO_2 nanofibers[23,24], TiO_2[24], and UiO–66NH_2[25] have reported promising results for both Sb(III) and Sb(V) adsorption. However, readily available and cost-effective materials are required to remediate Sb from contaminated water.

Recently, biochar has received notable attention as environmentally friendly and effective adsorbents, cost-efficient materials for the remediation treatment of metal(loid)s[26]. Although several studies have documented Sb adsorption to pure minerals[27,28] and humic substances[29,30], very few studies of Sb sorption onto biochars have been reported to date[31,32]. Antimonate can strongly bind to $Fe(OH)_2$/$Fe(OH)_3$, but, the bonding environment is still not clearly resolved[33,34]. Similarly, little is currently known on the Sb sorption by biochars, sorption mechanisms and the possible surface transformations which may occur.

Biochars have been modified to improve the sorption properties for oxyanions such as Sb and As. For instance, one study investigated the elimination of Sb(III) using different metal oxide composites consisting of Fe and Mn[18]. Hydrous Zr–O is known to display ion exchange ability, and specific binding potentiality of Zr(IV) to different oxyanions due to its strong Zr(IV)–O bonds[35]. The excellent performance of Zr-based metal organic frameworks were presented in removing Sb and As from water[25]. Ren et al.[36] demonstrated the high removal capacity for As using Fe–Zr binary oxide. Being from the same group (group V), As and Sb share some similar properties, but also show contrasting interactions with Fe and organic moeities[30,37].

In this study, we report the Sb(V) removal with modified and unmodified biochars and potential redox transformations associated with biochar. The objectives of this study were to: (1) synthesise a series of Zr treated biochar, Zr–Fe treated biochar and Fe treated biochar by a co-precipitation method, and (2) evaluate the adsorption performance of Sb(V) in aqueous solution as controlled by solution pH, adsorbate dosage, reaction time, initial concentration, temperature, influence of major coexisting cations and anions, surface charge, and surface area. In addition, we explored the surface transformation of Sb(V) to Sb(III) under oxic conditions with X-ray photoelectron spectroscopy (XPS).

Results and discussion

Biochar characterization. The zeta potential of all biochars in the range of pH 2–11 varied between + 25.02 to – 35.54 mV (Table S1 in Supporting Information (SI) section). Increasing pH translated to increasing negative surface charge of pristine biochars. The net surface charge of modified Zr–$FeCl_3$BSBC(1:5) and Zr–FeBSBC(1:20) carried positive charge up to pH 5 and 6, whereas Zr–$BSBC_{6.5}$, Zr–$BSBC_{12.5}$, Fe–BSBC, and $FeCl_3$–BSBC carried a positive surface charge at pH < 3. At low pH, the net protonation from the medium was enough to balance the negative charge of all biochars. The iso-electric point was reached at pH 2–6 (Table S1). The physico-chemical characteristics and elemental composition of biochars are provided in Table S2 and Table S3, respectively.

The surface functional groups of modified biochars analyzed by FTIR are presented in Fig. 1. The most prominent, broad and strong bands occurred at around 3400 cm^{-1}, corresponding to the stretching and bending vibrations of –OH functional groups of tightly bonded water molecules (Fig. 1A)[31,32,38]. The peak at 1640 cm^{-1} was explained by the deformation of water molecules and indicated physio-sorbed H_2O on the adsorbent by oxide[32,36]. Previous studies also support this[39,40]. The spectra at around 2900 cm^{-1} could be attributed to CH_3– stretching which exists in all biochars; similar findings were reported by Vithanage et al.[32].

A spectral shift of 2915–2960 and 2845–2865 cm^{-1} occurred due to Zr and/or Fe modifications compared to the pristine biochar (Fig. 1A). The two spectrum bands at 3694 and 3791 cm^{-1} (Fig. 1A) ascribed to freely vibrating surface hydroxyl groups can be found in BSBC, FeBSBC and $FeCl_3$BSBC. However, after Zr-modification the bands shifted to 3646, 3671, and 3687 cm^{-1}, which is responsible for ZrO_2 monoclinic (Zr–OH) and tetragonal (Zr–OH–Zr) (Fig. 1A) crystalline super structure (tri-bridges OH– groups on Zr^{4+})[41]. Moreover, the band at 3746 cm^{-1} could arise from the SiO_2 group. The bands 1522, 1541, 1544, 1559, and 1574 cm^{-1} were due to Zr–OH vibrations[42] found in the Zr and/or Fe-modified BSBC. The Zr and P peaks always overlapped. In addition, peaks at 1315, 1339, 1343, 1397, 1418, and 1420 cm^{-1} (1300–1420 cm^{-1}) ascribed to carboxylate groups[36] were developed in Zr-modified biochars (Fig. 1B). This was due to the deformation vibration of Zr–OH. Samples reacted with Sb(V) demonstrated a new sharp band at 1384 cm^{-1} (Fig. 1C,D) which was not observed in unreacted biochars. The absorption band is attributed to the Sb–O bond. Another distinguishable feature is that the structure of the spectra at 795 cm^{-1} of Sb(V) reacted biochar was sharper than the Sb(V)-unreacted biochar (Fig. 1D).

Figure S1 shows representative SEM images of each of the biochars. Distinct micropores were observable, especially in the unmodified BSBC biochars. Figure S1(i–ii); and B(i–ii) to G(i–ii), represents the morphology and surface characteristics of pristine BSBC and different modified biochars, respectively, before the sorption of Sb(V) at two different magnifications. Similarly, Figure S1(iii), and 2B(iii)–G(iii) describes the morphology and surface texture of Sb-loaded pristine, and Sb-loaded modified biochar-composites, respectively, after sorption of Sb(V) from aqueous solution. The morphology and surface texture of modified biochars contrasted from one another, which were covered by high densities of fine Zr, or Zr–Fe particles. Moreover, some fractions of Zr(IV) were located randomly onto the biochar surface which indicates a heterogeneous coating of these metals occurred during co-precipitation [Figure S1 B(i)–E(i)].

The SEM–EDS spectrum of $ZrBSBC_{6.5}$, $ZrBSBC_{12.5}$, Zr–FeBSBC(1:20) and Zr–$FeCl_3$BSBC(1:5) confirmed the presence of Zr in the Zr and/or Zr–Fe-modified biochars at 2.042 keV [Figure S2 B(i)–E(i)]; and Figure S2 A(i), S2 F(i) and S2 G(i) represents the SEM–EDS of pristine BSBC, FeBSBC and $FeCl_3$BSBC, respectively. After sorption of Sb(V) onto these adsorbents and the characteristic peaks at 3.604 keV in the EDX spectra [Figure S2 A(ii)–G(ii)], this confirmed the existence of sorbed Sb(V) along with C, O, N, Fe, P, Sb, and Zr. However, SEM–EDS spectra of P (K-line 2.013 keV) and Zr (L-line 2.042 keV) in biochars may not be clearly differentiated due to their very close X-ray energy levels. Thus, overlapping spectra of P and Zr was observed. To overcome this issue, TEM–EDS was performed where the Zr K-line was confirmed at 15.744 keV and could be differentiated from the P K-line. The SEM–EDS analysis also provided evidence that Zr–FeBSBC (1:20) showed substantial
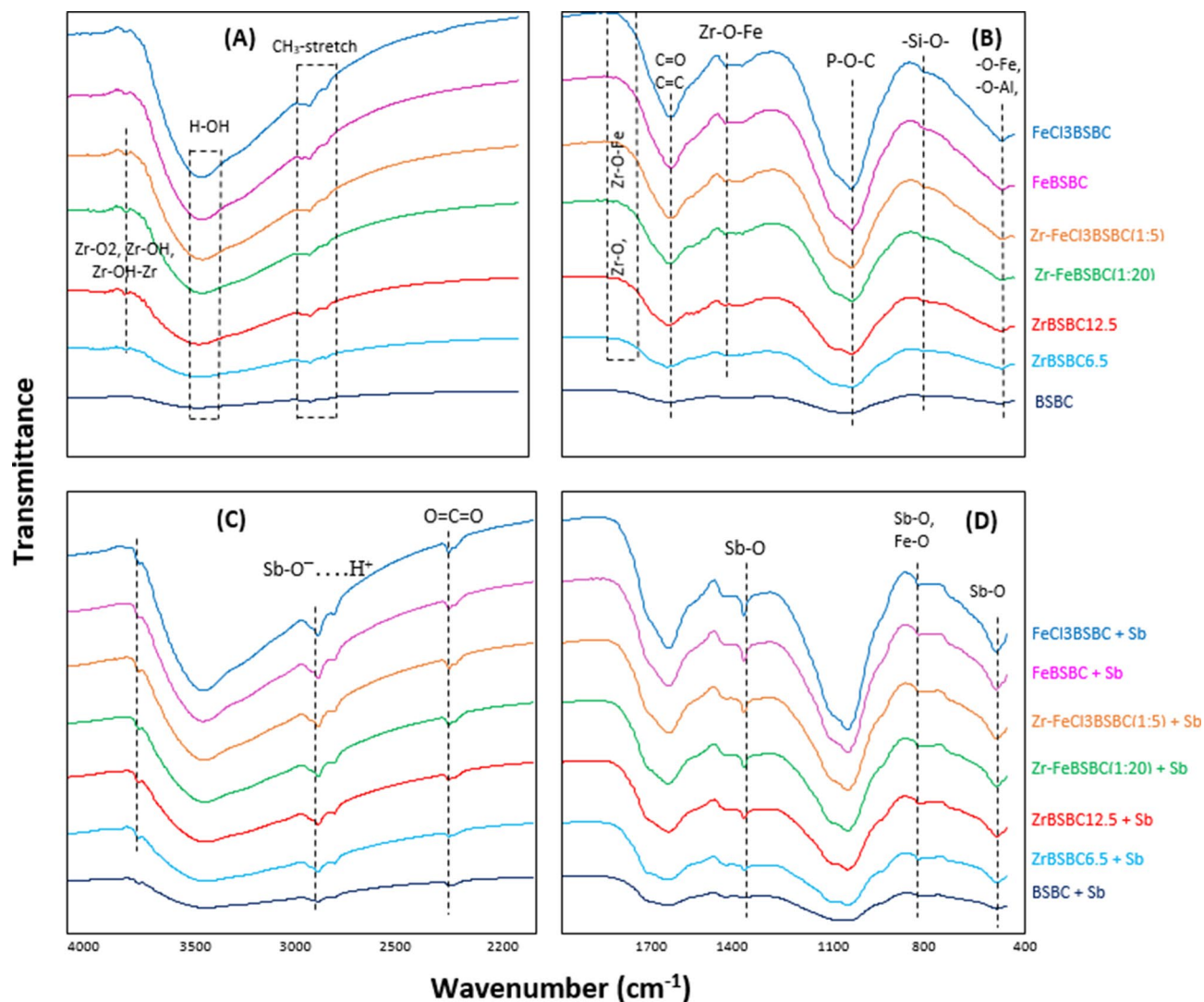
Figure 1. FTIR Spectra of biochars before (**A**, **B**) and after (**C**, **D**) Sb(V)-sorption.

wt. (%) distribution of Sb(V) (10.94 wt. %) than other biochars, indicating Zr–FeBSBC (1:20) possessed a high Sb(V) sorption efficiency.

The TEM images of pristine BSBC, ZrBSBC$_{12.5}$ and Zr–FeBSBC (1:20) are shown in Figure S3. Results from EDS–TEM elemental mapping indicated that C, O, Ca, P, Si, S, Ca, K, Mg, were the major elements in biochar structure, yet the intensity and brightness of C, O, P and Ca were more noticeable in pristine BSBC (Figure S3A). TEM elemental images also confirmed the presence of Zr and Zr–Fe in Zr–BBSC$_{12.5}$ and Zr–FeBSBC (1:20) (Figure S3C and S3D). The TEM–EDS spectrum of ZrBSBC$_{12.5}$ and Zr–FeBSBC (1:20) confirmed the presence of Zr (K-line) (mass percentage 15.06% and 2.79%, respectively) located heterogeneously on the biochar surfaces, suggesting the procedure successfully coated Zr with biochar at 2.042 keV (L-line) (Figure S4 in SI section). Characteristic Sb spectra were identified characteristics Sb spectra were found after sorption of Sb(V) with BSBC (Sb mass 15.44%), ZrBSBC$_{12.5}$ (Sb mass 3.45%, Zr mass 11.80%) and Zr–FeBSBC(1:20) (Sb mass 5.34%, Zr mass 0.73%) (see Figure S4 in SI Section). However, TEM images demonstrate different forms of non-uniform nanosized Zr and Sb crystals (Fig. 2). The lattice planes could be clearly sighted with a *d*-spacing at~0.35 nm, characteristic of the (111) plane of the Zr-crystalline tetragonal phase[43](Fig. 2). The formation of Sb crystal features on the biochar surfaces indicates surface modification and transformation of Sb to a possible 3-dimensional feature on the surface.

The results from XPS analysis similarly confirmed the transformation of Sb(V) at the surface of all biochars (Fig. 3). The two peaks of Sb 3d3 and Sb 3d5 are located at binding energies of 531.6 and 540.7 eV after sorption of Sb (Fig. 3A) which demonstrates the existence of both Sb(V) and Sb(III) species on the biochar surface. The appearance of two Sb peaks suggests that the reduction of Sb(V) to Sb(III) occurred during sorption by pristine BSBC as well as Zr-modified, Zr–Fe modified and Fe-modified biochars under oxidizing environments. Previous research on As has indicated redox transformations may occur during reaction with pyrolised organic materials, such as the surface of biochars[31]. Kappler et al.[44] demonstrated that biochar particles under reducing conditions acted as an electron shuttle, resulting in redox transformation of Fe and potentially other redox sensitive elements.
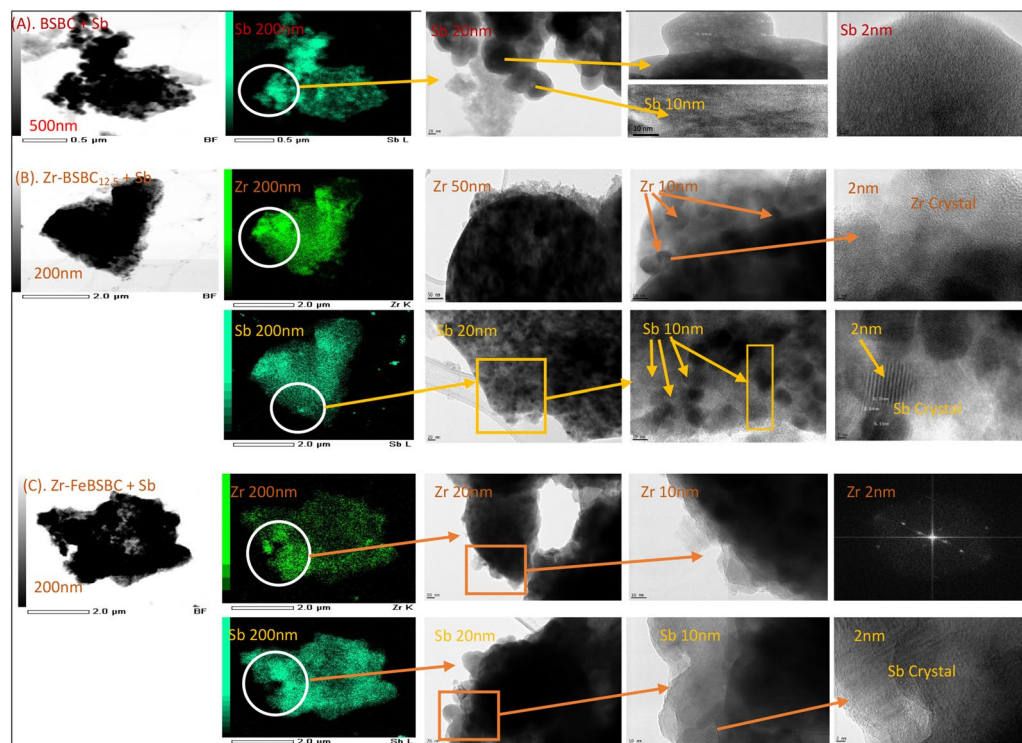
Figure 2. Different magnifications of Sb(V) and Zr onto Sb-loaded (**A**) BSBC, (**B**) ZrBSBC$_{12.5}$, and (**C**) Zr-FeCl$_3$BSBC biochars revealed by TEM imaging (Zr and Sb-crystallinity).

The current work indicates, that even under oxidizing conditions, biochar surfaces may promote reductive transformation of Sb during reaction, whether modified with Zr (Fig. 3B) or Fe (Fig. 3D).

The O$_{ad}$/O$_{latt}$ ratio increased from 1.0 to 1.21 and 1.0 to 1.11 from BSBC to ZrBSBC$_{12.5}$ and FeBSC after Sb sorption, respectively. However, this ratio decreased to 0.55 in Zr–FeBSBC(1:20) due to the incorporation of additional Fe association with Zr. In addition, the Fe content decreased from 0.51 to 0.17 at % for ZrBSBC$_{12.5}$ compared to pristine BSBC. Interestingly, the Fe content increased for Zr–Fe (0.51–0.56 at.%) and Fe-modified (0.51–0.66 at.%) biochars compared to pristine biochar. Therefore, the Zr–O, Zr–O–Fe or Fe–O site play significant role for enhanced Sb sorption by Zr–BSBC, Zr–FeBSBC and FeBSBC.
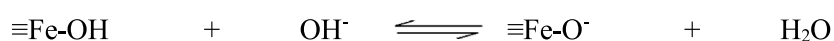
The chemical composition of pristine BSBC, ZrBSBC$_{12.5}$, Zr–FeBSBC (1:20) and FeBSBC after Sb(V) sorption was characterized by XPS. The XPS survey spectrum clearly showed the corresponding peaks to O 1 s (531.65 eV), N 1 s (400.21 eV), C 1 s (284.8 eV), P 2p (133.77 eV), Fe 2p (711.83), and Sb 3d (540.65 eV) (Figure S5). The XPS survey spectra confirmed the successful bonding of Zr onto ZrBSBC$_{12.5}$ (Zr3d5 at 182.76 and Zr 3d3 at 185.45 eV) and Zr–FeBSC (1:20) (Zr 3d5 at 183.17 and Zr 3d3 at 185.36 eV) surface (Fig. 3B,C). The two Zr 3d peaks can be observed at two binding energies and exists in (+) 4 oxidation state[45]. The peak at approximately 182.76 and 185.36 eV represent to the a Zr–O bonds while the peaks at approximately 182.81 and 185.36 eV correspond to the metallic Zr bonds (Zr–Zr) which was slightly shifted by loading of Sb (Fig. 3B,C)[13].

Antimonate sorption to biochars. *Effect of pH.* The highest adsorption (85–96%) appeared at a broader range of pH 2–6 for modified Zr–FeBSBC (1:20) and Zr–FeCl$_3$BSBC (1:5), whereas for pristine BSBC the rates were low between pH 3 and 8, which sharply declined at pH 8 (25%) (Fig. 4A).

At pH < 5, the biochar composites behave as weak acids and formed positivity charged surfaces sites. Since most of the metallic oxides/hydroxides demonstrated amphoteric surface characteristics, the Zr/Fe oxides could be protonated at acidic pH by the following reactions:

$$\equiv\!Zr\text{-}OH \quad + \quad H^+ \quad \rightleftharpoons \quad \equiv\!Zr\text{-}OH_2^+$$

$$\equiv\!Fe\text{-}OH \quad + \quad H^+ \quad \rightleftharpoons \quad \equiv\!Fe\text{-}OH_2^+$$

The Zr/Fe oxides could be deprotonated at basic pH by the following reactions:

$$\equiv\!Zr\text{-}OH \quad + \quad OH^- \quad \rightleftharpoons \quad \equiv\!Zr\text{-}O^- \quad + \quad H_2O$$

$$\equiv\!Fe\text{-}OH \quad + \quad OH^- \quad \rightleftharpoons \quad \equiv\!Fe\text{-}O^- \quad + \quad H_2O$$
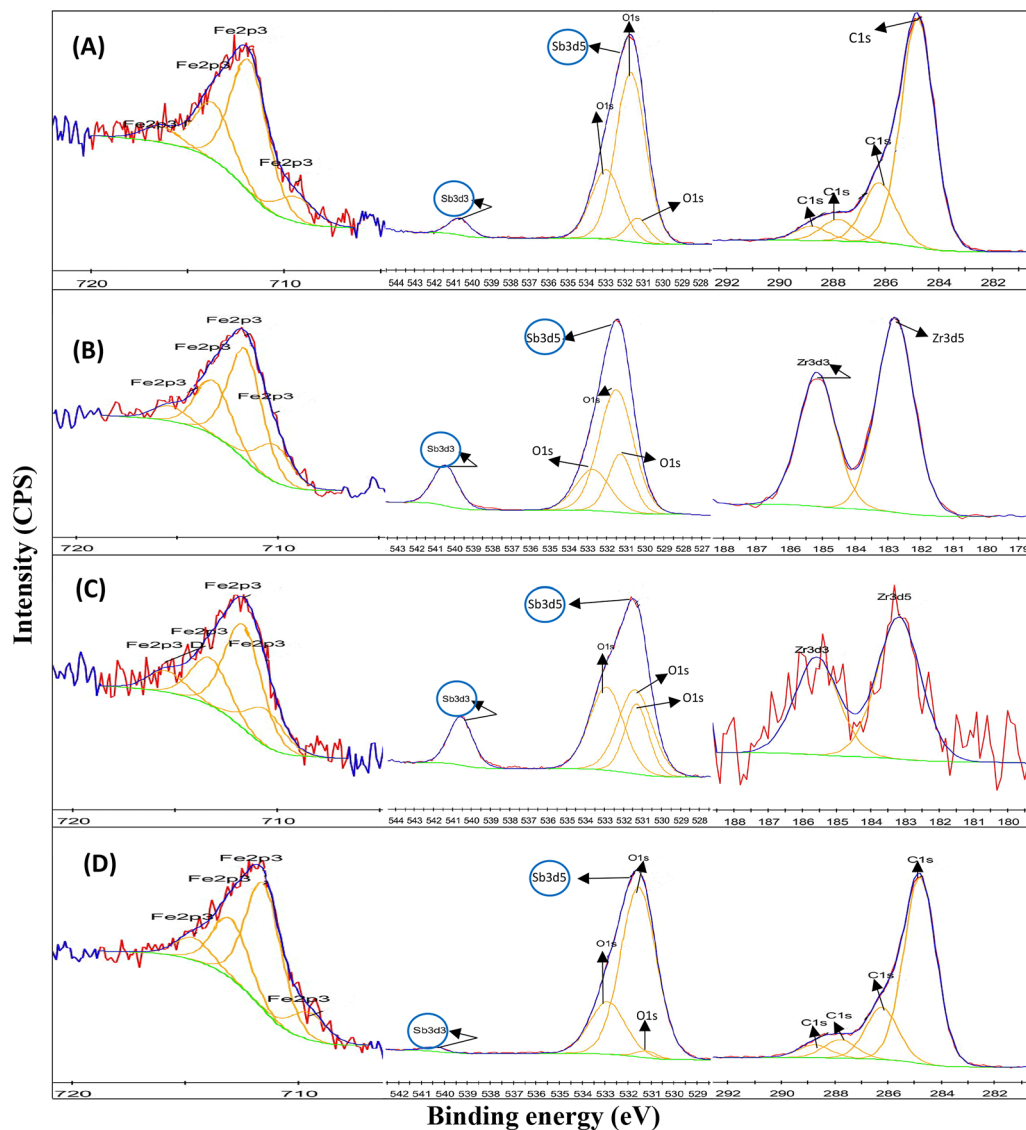
Figure 3. XPS expanded peaks of Sb-loaded BSBC (**A**), ZrBSBC12.5 (**B**), Zr-FeBSBC(1:20) (**C**) and FeBSBC (**D**).
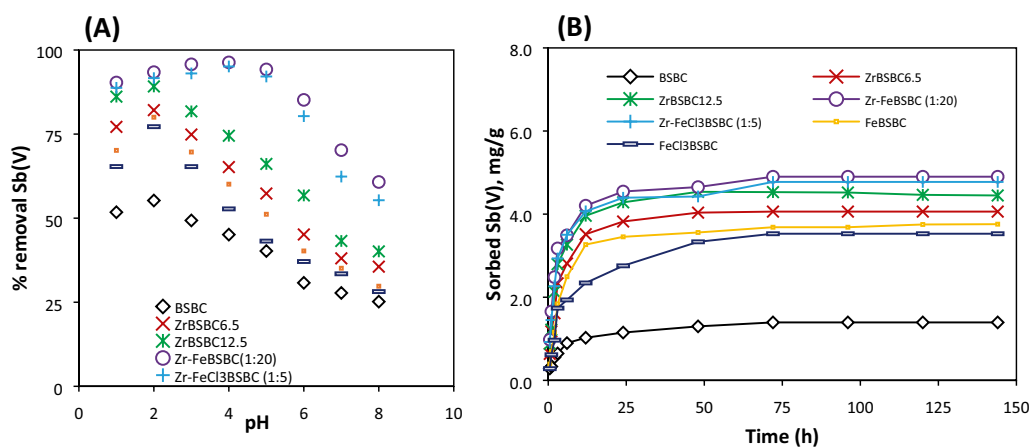

Figure 4. Effect of pH on removal percentage (%) of Sb(V), (**A**) [Initial concentration was 20 mg/L Sb(V), biochar dosage was 4 g/L, temperature was 22 °C] and effect of time on sorption capacity of Sb(V), (**B**) [Initial concentration 5 mg/L for BSBC, and 20 mg/L for ZrBSBC$_{6.5}$, ZrBSBC$_{12.5}$, Zr-FeBSBC(1:20), Zr-FeCl$_3$BSBC (1:5), Fe-BSBC and FeCl$_3$-BSBC Sb(V), biochar dosage was 4 g/L, temperature was 22 °C].

Biochar	q$_{e-exp}$ (mg/g)	Pseudo first-order			Pseudo second-order				Elovich			Intraparticle diffusion			
		k$_1$ (h^{-1})	q$_{e-cal}$	R^2	k$_2$ (g mg^{-1} h^{-1})	q$_{e-cal}$ (mg/g)	h (mg/g h)	R^2	β (mg/g)	α (mg/g.h)	R^2	k$_{id}$ (g mg^{-1} h$^{-1/2}$)	C (mg/g)	R^2	pH
BSBC	1.40	0.042	0.96	0.89	0.19	1.43	0.39	0.99	0.42	0.21	0.97	0.10	0.48	0.82	2
ZrBSBC6.5	4.06	0.065	1.50	0.89	0.10	4.15	1.75	0.99	1.56	0.57	0.90	0.26	1.65	0.70	2
ZrBSBC12.5	4.45	0.031	0.96	0.44	0.12	4.55	2.54	0.99	1.89	0.61	0.88	0.27	1.99	0.67	2
Zr–FeBSBC (1:20)	4.91	0.046	1.84	0.88	0.09	4.98	2.31	0.99	2.03	0.62	0.92	0.27	2.24	0.70	4
Zr–FeCl3B-SBC (1:5)	4.78	0.052	1.96	0.88	0.08	4.86	2.03	0.99	2.22	0.61	0.91	0.28	2.10	0.70	4
FeBSBC	3.76	0.046	2.05	0.94	0.07	3.85	1.05	0.99	1.10	0.60	0.90	0.26	1.25	0.71	3
FeCl3BSBC	3.53	0.063	2.27	0.89	0.05	3.69	0.67	0.99	0.78	0.60	0.97	0.27	0.91	0.83	2

Table 1. Kinetic models and fitted parameters for Sb(V) sorption data.

Thus the presence of Zr and/or Fe in the Sb(V) solution at different pH shows a buffering effect[46,47]. The adsorption capacity of Sb(V) did not change greatly up to pH 3. This might be due to the presence of undissociated Sb(V) species in the aqueous solution. Moreover, the pHzpc of BSBC, ZrBSBC$_{6.5}$, ZrBSBC$_{12.5}$, Zr–FeB-SBC(1:20), Zr–FeCl$_3$BSBC(1:5), Fe–BSBC and FeCl$_3$–BSBC were 3.6, 3.7, 3.8, 6.2, 5.7, 3.9 and 3.8, (Figure S6), and Sb(V) being in undissociated form at this pH range. This subsequently suggest a likely influence of electrostatic binding. Additionally, zeta potential measurements confirmed net negative biochar surfaces at pH > pH$_{pzc}$ (Figure S6). This explains the decrease in sorption capacity as the pH rises above pH$_{pzc}$.

Sorption kinetics. The kinetics data well fitted by the pseudo-second-order kinetics model (Table 1). Both pristine and modified biochars slowly adsorbed Sb(V) from aqueous solutions and reached equilibrium in 72 h (Fig. 4B). Antimonate sorption kinetics to biochars did not fit well with the first-order-kinetics and Elovich models. This is because the calculated q_e and experimentally observed q_e were extremely poor at initial Sb(V) concentration (Table 1 and Supporting Information). However, the kinetic data best fitted with the pseudo-second-order model with R^2 values ≥ 0.99 (Table 1). This indicates the likelihood of chemisorption processes and not purely electrostatic interactions between the adsorbent and adsorbate[48].

In this study, the initial linear part of the curve described the surface diffusion and the curve did not intersect through the origin (C ≠ 0) (Figure S7) suggesting that intra-particle diffusion was not the only rate controlling phase but more than one process controls the sorption. Here, Sb(V) uptake was observed in apparent two phases: a sharper linear component attributed to Sb(V) diffusion of Sb(V) species to ZrBSBC$_{6.5}$, ZrBSBC$_{12.5}$, Zr–FeBSBC (1:20), Zr–FeCl$_3$ (1:5), FeBSBC and FeCl$_3$BSBC through boundary layer diffusion, subsequently followed by intra-particle diffusion (Figure S7).

Sorption isotherms. The adsorption of Sb(V) by all modified biochars increased rapidly in the concentration range of 1–10 mg L^{-1} followed by a gradual increase thereafter (Fig. 5). Langmuir, Freundlich, Temkin and Dubinin–Radushkevich models were utilized to fit the experimental data (Table 2 and Fig. 5A–D). Despite the fact that all isotherms fitted well, the Freundlich and Dubinin–Radushkevich models reproduced Sb(V) sorption data overall to highest extent ($R^2 ≥ 0.99$). This indicates that multilayer sorption was a potential sorption process mechanism for Sb(V) (Table 2 and Fig. 5B,D). Freundlich constant K_F values spanned between 0.49 and 8.04 for all Sb(V) isotherm models with a slightly higher K_F obtained for ZrBSBC$_{12.5}$ than Zr–FeBSBC (1:20), respectively (Table 2). The sorption intensity or heterogeneity of a sorbent surface is indicated by the 1/n that reflects deviance from linearity. The 1/n values were in the order of Zr–FeBSBC (1:20) > Zr–FeCl$_3$BSBC (1:5) > Fe–BSBC > Zr–BSBC$_{6.5}$ > FeCl$_3$–BSBC > ZrBSBC$_{12.5}$ > BSBC; and spanned 0.583–0.813. This suggested that sorption process was favourable and chemical in nature belongs to the batch experimental conditions (Table 2)[31,49].

The maximum Sb(V) sorption capacities (q_m) of biochars followed the order Zr–FeBSBC (1:20) > Zr–FeCl$_3$B-SBC (1:5) > ZrBSBC$_{12.5}$ > ZrBSBC$_{6.5}$ > FeBSBC > FeCl$_3$BSBC > BSBC. The maximum sorption of Sb(V) observed for Zr–FeBSBC (1:20), Zr–FeCl$_3$BSBC (1:5), ZrBSBC$_{12.5}$, (98.04, 85.47 and 66.67 mg g^{-1}) followed by ZrBSBC$_{6.5}$, FeBSBC, FeCl$_3$BSBC, BSBC, (46.95, 39.68, 31.54, and 17.54 mg g^1), respectively (Fig. 5A and Table 2).

The R^2 value for the Temkin model of BSBC was 0.93. For modified biochars R^2 ranged from 0.91–0.98 (Table 2 and Fig. 5C). In the Dubinin–Radushkevich (D–R) model, R^2 values were 0.99 (Fig. 5D and Table 2) for pristine and modified biochars, and the higher theoretical sorption of modified biochars were ascribed to its greater micro-porosity and reduced pore diameter. This outcome agreed with the greater SSA of the modified biochars. The bonding energy E (kJ mol^{-1}) provides indirect data on the sorption mechanism, whether physical or chemical in nature. The calculated values between 8.57–9.20 kJ mol^{-1} indicate that the sorption system takes place chemically (chemisorption); values less than 8 kJ mol^{-1} indicate the system proceeds physically[50].

Effect of major anions, major cations and ionic strength. The widely occurring anions such as SO$_4$$^{2-}$, PO$_4$$^{3-}$ and CO$_3$$^{2-}$ have been revealed to exhibit different effects on the adsorption of Sb[17]. The Cl$^-$, NO$_3$$^-$, and SO$_4$$^{2-}$ did not pose any significant effect on Sb(V) sequestration because they have very minor affinities (between 3–6%) (Figure S8A). Carbonate showed little effect on the sorption of Sb(V) even at 1.0 M. The sorption capacity of
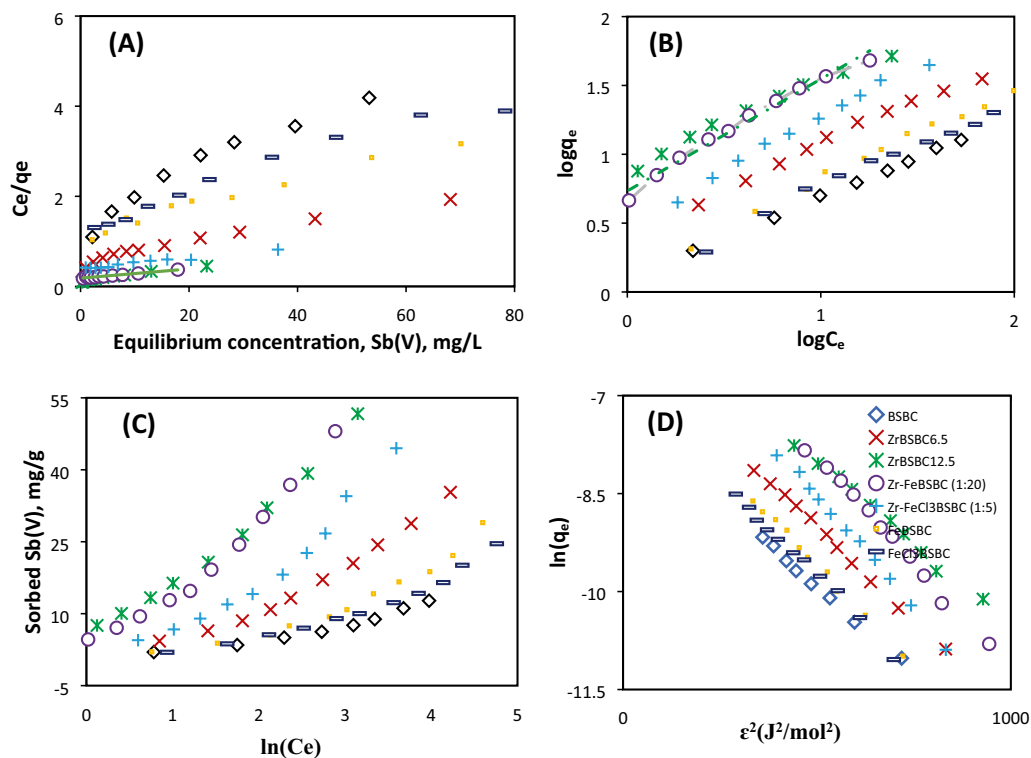
Figure 5. Isotherm model Langmuir (**A**), Freundlich (**B**), Temkin (**C**), and D–R (**D**) (Initial Sb(V) concentration was 5–250 mg/L, biochar density was 4 g/L at 22 °C).

Sb(V) decreased slightly (up to 12%) from 5.13 to 4.45 mg g^{-1} (96.44–84.07%) due to the presence of CO$_3^2$. It is possibly because the Cl$^-$, NO$_3^-$, CO$_3^{2-}$, SO$_4^{2-}$ anions could mainly form outer-sphere complexes with biochar and thus affected Sb(V) sorption to minimal extent[51]. Analogously, much more significant retardation of PO$_4^{3-}$ on Sb(V) sorption was observed, and the sorption capacity decreased (27%) from 4.73 to 3.46 mg g^{-1} (94.86–71.31%) (Figure S8A) even at 0.01 M PO$_4^{3-}$. The impact of PO$_4^{3-}$ was particularly evident in the Zr–FeBSBC (1:20), which similarly indicates a specific sorption mechanism in this adsorbent. These results were consistent with previous studies on the Sb(V) adsorption onto Ce(III)-doped Fe$_3$O$_4$ particles[46], magnetic sludge particles[52] and La-doped magnetic biochars[53]. In addition, PO$_4^{3-}$ may undergo inner-sphere complexation with oxy-hydroxide compounds and compete with the same sorption sites of the biochar composites. The influence of interfering major cations such as Na$^+$, K$^+$, Mg^{2+}, and Ca^{2+} of Sb(V) revealed that no notable changes in Sb(V) sorption (Figure S8B). In this study, a higher ionic strength significantly decreased the sorption capacity by 10.85% (3.37–3.04 mg/g), 19.23% (4.73–3.82 mg/g), 11.88% (5.05–4.45 mg/g), 6.35% (5.35–5.01 mg/g), 11.71% (5.12–4.52 mg/g), 17.18% (4.54–3.76 mg/g) and 14.85% (4.85–4.13 mg/g) for BSBC, ZrBSBC$_{6.5}$, ZrBSBC$_{12.5}$, Zr–FeBSBC(1:20), Zr–FeCl$_3$BSBC(1:5), FeBSBC, and FeCl$_3$BSBC, respectively, when NaNO$_3$ concentrations increased from 0.01–1.0 M (Figure S9A). At high concentrations, the NO$_3^-$ anion may compete with Sb(OH)$_6^-$ for the available sites on the biochar surface, and reduce Sb(V) reaction with the biochar[54,55]. However, as shown below, NO3$^-$ did not influence Sb(V) sorption. Secondly, Sb(V) exists mainly as highly polymerised hydroxyl-nitro complexes or colloidal hydrous oxides in the presence of high NO$_3^-$ concentrations[56]. In this research, 0.01 M NaNO$_3^-$ is considered as an ideal background electrolyte.

Chemistry of Sb(V) binding mechanisms onto biochars. Antimonate exists in solution predominantly as an anionic species and thus it is expected to bind to biochars largely via ion exchange and ligand exchange mechanisms. Broadly speaking, Sb(V) removal from an aqueous solution via sorption onto Zr–BSBC, Zr–FeBSBC and FeBSBC may be due to one or more factors such as: (1) electrostatic attraction, (2) nodule formation through hydrogen bonding, and (3) surface complexation or ligand exchange. Only at a pH < 2 does Sb(V) form positively charged species to any significant degree. Also, it can be assumed that at pH < 4, the biochar composites should behave as weak acids and a net positive surface charge predominated. The ZP and pH$_{PZC}$ of BSBC, ZrBSBC$_{6.5}$, ZrBSBC$_{12.5}$, Zr–FeBSBC, Zr–FeCl$_3$BSBC, Fe–BSBC and FeCl$_3$–BSBC confirmed a positive in this pH range. Antimonate being in an undissociated form in the pH < pH$_{PZC}$, an important sorption mechanism between the aqueous Sb(OH)$_6^-$ species is likely to be electrostatic attraction. The Zr content in ZrBSBC plays an important role in increasing Sb(V) sorption. However, the presence of Zr and Fe resulted in the greatest removal of Sb(V) from the solution. The presence of Zr and Fe resulted in the greatest removal of Sb(V) from the solution. This may be due to the enhanced SSA (specific surface area) from the Zr–Fe coatings on biochar surface and an increase in the positive surface charge produced compared to pristine biochar, which is responsible for higher Sb uptake. Thermodynamic results demonstrated that Sb(V) sorption was more favourable with an increase in temperature

Biochar	q_{exp} (mg/g)	Langmuir model parameters					Freundlich model parameters				Temkin model parameters			Dubinin–Radushkevich model parameters				pH
		q_{cal} (mg/g)	q_m (mg/g)	K_L (L mg^{-1})	R_L	R^2	q_{cal} (mg/g)	K_F (g mg^{-1} h^{-1})	$1/n$	R^2	b (J/mol)	A (L/g)	R^2	q_m (mg/g)	E (kJ mol^{-1})	β	R^2	
BSBC	12.71	12.07	17.54	0.041	0.18–0.69	0.95	12.90	1.27	0.584	0.99	731.6	0.56	0.93	80.23	9.80	5.2×10^{-3}	0.99	2
ZrB-SBC$_{6.5}$	35.31	34.10	46.95	0.039	0.11–0.71	0.98	39.92	2.719	0.636	0.99	261	0.46	0.96	253.26	9.36	5.7×10^{-3}	0.99	2
ZrB-SBC$_{12.5}$	51.68	49.45	66.67	0.123	0.03–0.44	0.97	57.83	8.039	0.627	0.98	177.45	1.23	0.98	508.96	9.90	5.1×10^{-3}	0.99	2
Zr–FeB-SBC (1:20)	47.12	41.60	−31.8	−0.033	1.52–0.16	0.54	33.89	0.910	1.271	0.92	153.94	0.39	0.63	4395	6.93	1.0×10^{-2}	0.90	2
	48.81	47.07	−60.61	−0.037	4.0–0.14	0.67	42.58	1.986	1.248	0.97	116.26	0.49	0.81	3202	7.58	8.7×10^{-3}	0.96	3
	48.04	48.84	98.04	0.055	0.077–0.63	0.96	56.56	5.41	0.8128	0.98	162.64	1.01	0.96	1120	9.77	6.5×10^{-3}	0.99	4
Zr–FeCl$_3$B-SBC (1:5)	38.80	36.40	70.42	0.011	0.89–0.29	0.96	31.43	1.633	0.796	0.99	251.55	0.42	0.89	456	8.45	7.0×10^{-3}	0.99	2
	44.16	37.64	125	0.014	0.87–0.25	0.49	39.20	1.929	0.883	0.99	173.58	0.37	0.86	644	8.45	7.0×10^{-3}	0.98	3
	44.49	44.47	85.47	0.029	0.13–0.76	0.97	50.08	3.12	0.772	0.99	185.73	0.54	0.93	727	9.57	6.8×10^{-3}	0.99	4
	47.36	35.44	112.36	0.017	0.85–0.21	0.20	35.81	2.139	0.857	0.94	229.9	0.51	0.82	274	9.62	5.4×10^{-3}	0.93	5
FeBSBC	39.80	32.91	120.48	0.006	0.93–0.41	0.35	32.16	1.13	0.833	0.99	260.03	0.32	0.76	325	8.45	7.0×10^{-3}	0.98	2
	28.98	26.51	39.68	0.02	0.18–0.83	0.95	30.29	1.36	0.6739	0.99	365.14	0.35	0.91	181	8.98	6.2×10^{-3}	0.99	3
	41.26	36.53	49.26	0.071	0.006–0.57	0.91	43.39	4.684	0.603	0.88	238.79	0.86	0.93	444	9.21	5.9×10^{-3}	0.93	4
FeCl$_3$B-SBC	41.76	34.67	270.27	0.003	0.96–0.57	0.21	35.16	1.0139	0.9447	0.99	216.26	0.31	0.80	799	7.71	8.4×10^{-3}	0.99	2
	24.60	22.66	31.54	0.022	0.17–0.81	0.95	26.08	1.313	0.6279	0.98	432.41	0.34	0.92	135	9.20	5.9×10^{-3}	0.99	3

Table 2. Sorption isotherm models and best-fit parameters for Sb(V) sorption data.

Biochar	ΔG (kJ mol^{-1})						ΔH (kJ mol^{-1})	ΔS (Kl/mol.K)	R^2	pH
	277 K	288 K	293 K	298 K	303 K	310 K				
BSBC	2.92	1.54	−0.29	−0.71	−1.71	−2.83	52.8	0.18	0.98	2
ZrBSBC$_{6.5}$	1.58	−0.23	−0.48	−1.83	−2.57	−3.19	43.1	0.15	0.98	2
ZrBSBC$_{12.5}$	−0.08	−1.31	−1.97	−2.78	−3.68	−4.54	38.3	0.14	0.99	2
Zr–FeBSBC (1:20)	−0.78	−2.52	−3.86	−4.66	−5.67	−7.26	53.7	0.2	0.99	4
Zr–FeCl$_3$BSBC (1:5)	−0.36	−1.79	−2.48	−3.37	−4.67	−5.72	45.7	0.16	0.98	4
FeBSBC	−0.27	−1.45	−2.07	−2.42	−2.71	−3.41	25.6	0.09	0.99	3
FeCl$_3$BSBC	0.67	−0.10	−0.37	−1.14	−1.94	−2.98	31.43	0.11	0.95	3

Table 3. Thermodynamic parameters for the sorption of Sb(V) on biochars.

which suggested chemisorption (surface complexation) (Table 3 and Figure S9B). The empty d-orbitals on Zr and Fe might facilitate the complexation of Sb(V) through the formation of inner-sphere Zr–O–Sb, Zr–O–Fe–Sb, and Fe–O–Sb complex or via hydrogen bonding. Results from TEM and XPS demonstrate surfaced induced changes in the Sb oxidation state. TEM images suggest a concentration of Sb or potential surface precipitation on the biochars. In addition, despite the experimental systems being open to the atmosphere (i.e. oxic), XPS analysis indicates substantial surface-induced reduction of Sb(V). Biochar has previously been implicated in serving as an electron shuttle, allowing potentially for chemically induced transformation of oxidized species[31,44,49]. The presence of Sb(III) and Sb-enriched crystalline materials suggest more complex surface processes than adsorption or homogenous precipitation mechanisms in pristine, Fe or Zr modified biochars. Especially under acidic conditions, the reduction of Sb(V) to Sb(III) may indicate the surface-induced precipitation of SbO$_3$. In this study, the hypothesis could not be confirmed. Nevertheless, the surface reduction of Sb(V) under oxic conditions has important implications for the application of biochars in contaminated waters or soils, due to the difference in toxicity and sorption behaviour.

Materials and methods

Preparation of pristine biochar. Pristine biochar was produced from biosolids. The feedstock was air-dried, ground (< 1 mm, 50 mesh), and heated in a muffle furnace followed by placing in a ceramic crucible under an N_2 atmosphere. The heating rate of 7 °C min^{-1} was employed using slow pyrolysis with holding at a peak temperature of 300 °C for 30 min[32]. The resulting biosolid biochar (BSBC) samples were cooled at room temperature inside the furnace. Afterwards, the BSBC was removed from the furnace, stored in airtight plastic containers and preserved in a desiccator for further experiments.

Modification of biochar. The Zr–BSBC composites were synthesized by employing an *in-situ* precipitation method[49]. In this study, a solution containing 5.0 g of BSBC and 50 mL 0.1 M zirconium (IV) chloride solution ($ZrOCl_2.8H_2O$) was brought to: i) pH 6.5 and ii) pH 12.5 through dropwise introduction of 0.1 M NaOH. The resulting suspension was aged for 12 h at room temperature. These two synthesized Zr–BSBC composites were rinsed several times by purified water to remove impurities after centrifugation at 5842 g for 15 min and followed by drying in an oven at 80 °C. The synthesized biochar composites (coded as Zr–BSBC$_{6.5}$ and Zr–BSBC$_{12.5}$) were preserved in a desiccator for further experiments.

Seven types of Zr–Fe and Zr–FeCl$_3$ biochar composites were synthesized from Fe chips and FeCl$_3$.6H$_2$O at pH 6.5. The Zr to Fe molar ratios were 1:1, 1:2, 1:5, 1:10, 1:20, 1:50 and 1:100. The biochar suspensions were shaken for 24 h and centrifuged at 5842 g for 15 min, followed by decanting. Then, the synthesized biochar composites were rinsed several times by purified water, centrifuged at 5842 g for 15 min and dried in an oven at 80 °C. In addition, a Fe-only modified biochar was produced from iron chips (Fe–BSBC) and iron chloride (FeCl$_3$–BSBC) as described above.

Characterization of adsorbents. Surface charge was characterised viz. zeta potential (ZP), point of zero charge (pH$_{PZC}$) and cation exchange capacity (CEC) using a NanoPlus HD analyser (Micromeritics, USA), Brunauer–Emmett–Teller (BET) for specific surface area (SSA). Pore size distribution and pore volume were determined using N_2 sorption (Tristar II 3020, Micromeritics, USA) and the elemental composition (C, N, S) measured using a LECO TruMac C/N/S. The surface functional groups and morphology was investigated with Fourier transform infrared (FT-IR, Agilent Cary 600), X-ray diffraction (XRD, Empyrean, PANanalytical) and Environmental Scanning Electron Microscopy (SEM, Zeiss Sigma, Germany) equipped with a Bruker energy dispersive X-ray spectroscopy (EDS) detector. Additionally, the micromorphology of biochar samples were determined using a high-resolution transmission electron microscope (HRTEM, JEM-2100F, Japan) coupled with EDS detector (JEOL-JED-2300). Antimony in all aqueous samples was determined by using inductively coupled plasma optical emission spectrometry (ICP-OES, PerkinElmer Avio 200, USA). The elemental oxidation number, surface composition and speciation of sorbed Sb on the biochars surface also determined by XPS (ESCALAB250Xi, Thermo Scientific, UK, mono-chromated Al K alpha).

Batch sorption experiments: pH, adsorption kinetics, and isotherms. Sorption edge investigations were achieved in the pH range of 1–10 at an initial Sb(V) concentrations of 10 mg L^{-1} with a biochar density of 4 g L^{-1} at room temperature (20 ± 2 °C). The suspension pH was controlled by addition 0.1 M HNO$_3$ and/or 0.1 M NaOH. Kinetics studies were conducted using 0.1 g biochar in 25 mL solution (biochar to solution ratio = 1:250), which was added to 50 mL falcon tubes containing 5 mg/L Sb(V) for 7 d at room temperature (22 ± 0.2 °C). The background electrolyte was 0.01 M NaNO$_3$ in ultrapure water. Following reactions, suspensions were centrifuged at 5842 g for 20 min and the supernatants were filtered through 0.22 μm PES filters. Kinetic data were fitted with four classical kinetic models, namely the pseudo-first-order kinetic model, pseudo-second-order kinetic model, Elovich model and Intra-particle diffusion model.

Adsorption isotherms used a similar procedure as the kinetic experiments except using a range of Sb(V) concentrations (5–250 mg L^{-1}) for 72 h at pH 2–10. Four sorption isotherm models were fitted to the data, namely the Langmuir, Freundlich, Temkin and Dubinin–Radushkevich models (detailed information of all isotherm models in SI section).

Influence of biochar dosage, interfering ions, ionic strength and thermodynamics. To assess the impact of adsorbent dosage on Sb(V) sorption, different dosages of biochar (solid:solution) (1:100, 1:250, 1:500 and 1:1000) were added into 50 mL centrifuge tubes maintaining pH at 2–10. Ionic strength (0.01, 0.1, 0.5 and 1.0 M of NaNO$_3$), coexisting anions (Cl$^-$, NO$_3^-$, SO$_4^{2-}$, CO$_3^{2-}$ and PO$_4^{3-}$ at concentrations of 0.01–0.1 M) and cations (0.1 M of Na, K, Mg, and Ca) were also studied. The pH of biochar samples were adjusted to 2.0 for BSBC, ZrBSBC$_{6.5}$, ZrBSBC$_{12.5}$, FeBSBC and 3.0 for Zr–FeBSBC (1:20), Zr–FeCl3BSBC (1:5), FeCl$_3$BSBC, respectively. The Sb(V) concentration was 20 mg/L, adding 0.1 g biochar in 25 mL solution. The thermodynamic studies were conducted by varying temperatures at 4, 15, 20, 25, 30, and 37 °C. The thermodynamic parameters of the Gibbs free energy (ΔG), entropy (ΔS), and enthalpy (ΔH) and were calculated (details are provided in SI section).

References

1. Filella, M., Belzile, N. & Chen, Y.-W. Antimony in the environment: a review focused on natural waters: I. Occurrence. *Earth-Sci. Rev.* **57**, 125–176 (2002).
2. Okkenhaug, G. *et al.* Antimony (Sb) and Arsenic (As) in Sb mining impacted paddy soil from Xikuangshan, China: differences in mechanisms controlling soil sequestration and uptake in rice. *Environ. Sci. Technol.* **46**, 3155–3162. https://doi.org/10.1021/es2022472 (2012).
3. Wang, X., He, M., Xi, J. & Lu, X. Antimony distribution and mobility in rivers around the world's largest antimony mine of Xikuangshan, Hunan Province, China. *Microchem. J.* **97**, 4–11. https://doi.org/10.1016/j.microc.2010.05.011 (2011).
4. Wu, Z., He, M., Guo, X. & Zhou, R. Removal of antimony (III) and antimony (V) from drinking water by ferric chloride coagulation: competing ion effect and the mechanism analysis. *Sep. Purif. Technol.* **76**, 184–190. https://doi.org/10.1016/j.seppur.2010.10.006 (2010).
5. Ungureanu, G., Santos, S., Boaventura, R. & Botelho, C. Arsenic and antimony in water and wastewater: overview of removal techniques with special reference to latest advances in adsorption. *J. Environ. Manag.* **151**, 326–342 (2015).
6. Mitsunobu, S., Takahashi, Y., Terada, Y. & Sakata, M. Antimony(V) incorporation into synthetic ferrihydrite, goethite, and natural iron oxyhydroxides. *Environ. Sci. Technol.* **44**, 3712–3718. https://doi.org/10.1021/es903901e (2010).
7. Mitsunobu, S., Takahashi, Y., Terada, Y. & Sakata, M. Antimony (V) incorporation into synthetic ferrihydrite, goethite, and natural iron oxyhydroxides. *Environ. Sci. Technol.* **44**, 3712–3718 (2010).
8. Filella, M., Williams, P. A. & Belzile, N. Antimony in the environment: knowns and unknowns. *Environ. Chem.* **6**, 95–105 (2009).
9. Gebel, T. Arsenic and antimony: comparative approach on mechanistic toxicology. *Chem. Biol. Interact.* **107**, 131–144 (1997).
10. IARC, (International agency for research on cancer). IARC Monographs on the Evaluation of Carcinogenic Risks to Humans. IARC Monogr. 831,Vol. 85 (2004). https://monographs.iarc.who.int/wp-content/uploads/2018/06/mono85.pdf
11. Guo, X. *et al.* Adsorption of antimony onto iron oxyhydroxides: adsorption behavior and surface structure. *J. Hazard. Mater.* **276**, 339–345 (2014).
12. Luo, F., Yang, D., Chen, Z., Megharaj, M. & Naidu, R. The mechanism for degrading Orange II based on adsorption and reduction by ion-based nanoparticles synthesized by grape leaf extract. *J. Hazard. Mater.* **296**, 37–45. https://doi.org/10.1016/j.jhazmat.2015.04.027 (2015).
13. Luo, J. *et al.* Removal of antimonite (Sb (III)) and antimonate (Sb (V)) from aqueous solution using carbon nanofibers that are decorated with zirconium oxide (ZrO2). *Environ. Sci. Technol.* **49**, 11115–11124 (2015).
14. Salam, M. A. & Mohamed, R. M. Removal of antimony (III) by multi-walled carbon nanotubes from model solution and environmental samples. *Chem. Eng. Res. Des.* **91**, 1352–1360 (2013).
15. Miao, Y. *et al.* Antimony (V) removal from water by hydrated ferric oxides supported by calcite sand and polymeric anion exchanger. *J. Environ. Sci.* **26**, 307–314 (2014).
16. Leng, Y., Guo, W., Su, S., Yi, C. & Xing, L. Removal of antimony (III) from aqueous solution by graphene as an adsorbent. *Chem. Eng. J.* **211**, 406–411 (2012).
17. Wang, L. *et al.* Mechanism of enhanced Sb(V) removal from aqueous solution using chemically modified aerobic granules. *J. Hazard. Mater.* **284**, 43–49. https://doi.org/10.1016/j.jhazmat.2014.10.041 (2015).
18. Xu, W., Wang, H., Liu, R., Zhao, X. & Qu, J. The mechanism of antimony(III) removal and its reactions on the surfaces of Fe–Mn Binary Oxide. *J. Colloid Interface Sci.* **363**, 320–326. https://doi.org/10.1016/j.jcis.2011.07.026 (2011).
19. Biswas, B. K., Inoue, J.-I., Kawakita, H., Ohto, K. & Inoue, K. Effective removal and recovery of antimony using metal-loaded saponified orange waste. *J. Hazard. Mater.* **172**, 721–728 (2009).
20. Xi, J., He, M. & Lin, C. Adsorption of antimony(III) and antimony(V) on bentonite: Kinetics, thermodynamics and anion competition. *Microchem. J.* **97**, 85–91. https://doi.org/10.1016/j.microc.2010.05.017 (2011).
21. Saeidnia, S., Asadollahfardi, G. & Khodadadi Darban, A. Simulation of adsorption of antimony on zero-valent iron nanoparticles coated on the industrial minerals (kaolinite, bentonite and perlite) in mineral effluent. *Desalination Water Treat.* **57**, 22321–22328 (2016).
22. Zou, J. P. *et al.* Three-dimensional reduced graphene oxide coupled with Mn_3O_4 for highly efficient removal of Sb(III) and Sb(V) from Water. *ACS Appl. Mater. Interfaces.* **8**, 18140–18149. https://doi.org/10.1021/acsami.6b05895 (2016).
23. Luo, J. *et al.* Antimony removal from aqueous solution using novel α-MnO2 nanofibers: equilibrium, kinetic, and density functional theory studies. *ACS Sustain. Chem. Eng.* **5**, 2255–2264 (2017).
24. Yan, L., Song, J., Chan, T. & Jing, C. Insights into antimony adsorption on TiO_2: XAFS and DFT study. *Environ. Sci. Technol.* **51**, 6335–6341. https://doi.org/10.1021/acs.est.7b00807 (2017).
25. He, X., Min, X. & Luo, X. Efficient removal of antimony (III, V) from contaminated water by amino modification of a zirconium metal–organic framework with mechanism study. *J. Chem. Eng. Data* **62**, 1519–1529 (2017).
26. Amen, R. *et al.* A critical review on arsenic removal from water using biochar-based sorbents: the significance of modification and redox reactions. *Chem. Eng. J.* **396**, 125195. https://doi.org/10.1016/j.cej.2020.125195 (2020).
27. Leuz, A.-K., Mönch, H. & Johnson, C. A. Sorption of Sb(III) and Sb(V) to goethite: influence on Sb(III) oxidation and mobilization. *Environ. Sci. Technol.* **40**, 7277–7282. https://doi.org/10.1021/es061284b (2006).
28. He, X. *et al.* Exceptional adsorption of arsenic by zirconium metal-organic frameworks: engineering exploration and mechanism insight. *J. Colloid Interface Sci.* **539**, 223–234 (2019).
29. Buschmann, J. & Sigg, L. Antimony (III) binding to humic substances: influence of pH and type of humic acid. *Environ. Sci. Technol.* **38**, 4535–4541 (2004).
30. Karimian, N., Burton, E. D. & Johnston, S. G. Antimony speciation and mobility during Fe(II)-induced transformation of humic acid-antimony(V)-iron(III) coprecipitates. *Environ. Pollut.* **254**, 113112. https://doi.org/10.1016/j.envpol.2019.113112 (2019).
31. Niazi, N. K. *et al.* Arsenic removal by perilla leaf biochar in aqueous solutions and groundwater: an integrated spectroscopic and microscopic examination. *Environ. Pollut.* **232**, 31–41. https://doi.org/10.1016/j.envpol.2017.09.051 (2018).
32. Vithanage, M. *et al.* Mechanisms of antimony adsorption onto soybean stover-derived biochar in aqueous solutions. *J. Environ. Manag.* **151**, 443–449. https://doi.org/10.1016/j.jenvman.2014.11.005 (2015).
33. Ambe, S. Adsorption kinetics of antimony (V) ions onto α-ferric oxide surfaces from an aqueous solution. *Langmuir* **3**, 489–493 (1987).
34. Scheinost, A. C. *et al.* Quantitative antimony speciation in shooting-range soils by EXAFS spectroscopy. *Geochim. Cosmochim. Acta* **70**, 3299–3312 (2006).
35. Wu, H. *et al.* Unusual and highly tunable missing-linker defects in zirconium metal-organic framework UiO-66 and their important effects on gas adsorption. *J. Am. Chem. Soc.* **135**, 10525–10532. https://doi.org/10.1021/ja404514r (2013).
36. Ren, Z., Zhang, G. & Paul Chen, J. Adsorptive removal of arsenic from water by an iron–zirconium binary oxide adsorbent. *J. Colloid Interface Sci.* **358**, 230–237. https://doi.org/10.1016/j.jcis.2011.01.013 (2011).
37. Burton, E. D., Hockmann, K. & Karimian, N. Antimony sorption to goethite: effects of Fe(II)-catalyzed recrystallization. *ACS Earth Space Chem.* **4**, 476–487. https://doi.org/10.1021/acsearthspacechem.0c00013 (2020).
38. Zhao, X. *et al.* Antimonate and antimonite adsorption by a polyvinyl alcohol-stabilized granular adsorbent containing nanoscale zero-valent iron. *Chem. Eng. J.* **247**, 250–257 (2014).

39. Bollino, F., Armenia, E. & Tranquillo, E. Zirconia/hydroxyapatite composites synthesized via Sol-Gel: Influence of hydroxyapatite content and heating on their biological properties. *Materials* **10**, 757 (2017).
40. Testa, M. L. *et al.* Use of zirconium phosphate-sulphate as acid catalyst for synthesis of glycerol-based fuel additives. *Catalysts* https://doi.org/10.3390/catal9020148 (2019).
41. Merle-Mejean, T., Barberis, P., Othmane, S. B., Nardou, F. & Quintard, P. Chemical forms of hydroxyls on/in zirconia: an FT-IR study. *J. Eur. Ceram. Soc.* **18**, 1579–1586 (1998).
42. Dou, X., Mohan, D., Pittman, C. U. Jr. & Yang, S. Remediating fluoride from water using hydrous zirconium oxide. *Chem. Eng. J.* **198**, 236–245 (2012).
43. Hang, C., Li, Q., Gao, S. & Shang, J. K. As(III) and As(V) adsorption by hydrous zirconium oxide nanoparticles synthesized by a hydrothermal process followed with heat treatment. *Ind. Eng. Chem. Res.* **51**, 353–361. https://doi.org/10.1021/ie202260g (2012).
44. Kappler, A. *et al.* Biochar as an electron shuttle between bacteria and Fe (III) minerals. *Environ. Sci. Technol. Lett.* **1**, 339–344 (2014).
45. Mallampati, R. & Valiyaveettil, S. Apple peels: a versatile biomass for water purification?. *ACS Appl. Mater. Interfaces.* **5**, 4443–4449 (2013).
46. Qi, Z., Joshi, T. P., Liu, R., Liu, H. & Qu, J. Synthesis of Ce (III)-doped Fe3O4 magnetic particles for efficient removal of antimony from aqueous solution. *J. Hazard. Mater.* **329**, 193–204 (2017).
47. Zheng, Y. M., Lim, S. F. & Chen, J. P. Preparation and characterization of zirconium-based magnetic sorbent for arsenate removal. *J. Colloid Interface Sci.* **338**, 22–29. https://doi.org/10.1016/j.jcis.2009.06.021 (2009).
48. Tian, Y. *et al.* Electrospun membrane of cellulose acetate for heavy metal ion adsorption in water treatment. *Carbohyd. Polym.* **83**, 743–748. https://doi.org/10.1016/j.carbpol.2010.08.054 (2011).
49. Rahman, M. A. *et al.* Removal of arsenate from contaminated waters by novel zirconium and zirconium-iron modified biochar. *J. Hazard. Mater.* https://doi.org/10.1016/j.jhazmat.2020.124488 (2020).
50. Sarı, A., Şahinoğlu, G. N. R. & Tüzen, M. Antimony (III) adsorption from aqueous solution using raw perlite and Mn-modified perlite: equilibrium, thermodynamic, and kinetic studies. *Ind. Eng. Chem. Res.* **51**, 6877–6886 (2012).
51. Cumbal, L. & SenGupta, A. K. Arsenic removal using polymer-supported hydrated iron (III) oxide nanoparticles: role of Donnan membrane effect. *Environ. Sci. Technol.* **39**, 6508–6515 (2005).
52. Wang, L. *et al.* Highly efficient As(v)/Sb(v) removal by magnetic sludge composite: synthesis, characterization, equilibrium, and mechanism studies. *RSC Adv.* **6**, 42876–42884. https://doi.org/10.1039/c6ra06208c (2016).
53. Wang, L. *et al.* Enhanced antimonate (Sb(V)) removal from aqueous solution by La-doped magnetic biochars. *Chem. Eng. J.* **354**, 623–632. https://doi.org/10.1016/j.cej.2018.08.074 (2018).
54. Hayes, K. F., Papelis, C. & Leckie, J. O. Modeling ionic strength effects on anion adsorption at hydrous oxide/solution interfaces. *J. Colloid Interface Sci.* **125**, 717–726 (1988).
55. Leuz, A.-K., Mönch, H. & Johnson, C. A. Sorption of Sb (III) and Sb (V) to goethite: influence on Sb (III) oxidation and mobilization. *Environ. Sci. Technol.* **40**, 7277–7282 (2006).
56. Filella, M., Belzile, N. & Chen, Y.-W. Antimony in the environment: a review focused on natural waters: II. Relevant solution chemistry. *Earth-Sci. Rev.* **59**, 265–285 (2002).

Acknowledgements

Author contributions

A.R.: Conceptualisation, Methodology, Formal analysis, Writing Original Draft; D.L.: Conceptualisation, Reviewing, Editing, Resources & Supervision; M.M.R.: Reviewing, Editing & Supervision; M.M.B.: Reviewing, Editing & Supervision; P.S.: Reviewing, Editing & Supervision.

Competing interests

The authors declare no competing interests.

Additional information

Supplementary Information The online version contains supplementary material available at https://doi.org/10.1038/s41598-021-86978-6.

Correspondence and requests for materials should be addressed to D.L.

Reprints and permissions information is available at www.nature.com/reprints.

Publisher's note Springer Nature remains neutral with regard to jurisdictional claims in published maps and institutional affiliations.